



## Short communication

Facile synthesis of layered Zn<sub>2</sub>SnO<sub>4</sub>/graphene nanohybrid by a one-pot route and its application as high-performance anode for Li-ion batteries

Wentao Song, Jian Xie\*, Wenyue Hu, Shuangyu Liu, Gaoshao Cao, Tiejun Zhu, Xinbing Zhao

State Key Laboratory of Silicon Materials and Department of Materials Science and Engineering, Zhejiang University, Hangzhou 310027, China

## HIGHLIGHTS

- We synthesize Zn<sub>2</sub>SnO<sub>4</sub>-nanocrystal/graphene-nanosheet hybrid by an in situ route.
- The hybrid exhibits an improved electrochemical performance than bare Zn<sub>2</sub>SnO<sub>4</sub>.
- The graphene offers buffering, conducting, and immobilizing effects for Zn<sub>2</sub>SnO<sub>4</sub>.

## ARTICLE INFO

## Article history:

Received 25 May 2012

Received in revised form

17 November 2012

Accepted 24 November 2012

Available online 5 December 2012

## Keywords:

Graphene

Zinc stannate

Nanohybrid

Electrochemical performance

In situ route

## ABSTRACT

A Zn<sub>2</sub>SnO<sub>4</sub>-nanocrystals/graphene-nanosheets (Zn<sub>2</sub>SnO<sub>4</sub>/G) nanohybrid has been prepared by a facile in situ hydrothermal route using SnCl<sub>4</sub>·5H<sub>2</sub>O, ZnCl<sub>2</sub> and graphite oxide (GO) as the precursors and N<sub>2</sub>H<sub>4</sub>·H<sub>2</sub>O as the mineralizer and reducing agent. The formation of Zn<sub>2</sub>SnO<sub>4</sub> and the reduction GO occur simultaneously during the hydrothermal process. The Zn<sub>2</sub>SnO<sub>4</sub> nanocrystals are uniformly dispersed and immobilized by the graphene nanosheets reduced from GO. The direct restacking of the hydrophobic graphene sheets is inhibited by loading Zn<sub>2</sub>SnO<sub>4</sub> nanocrystals as the spacers. Zn<sub>2</sub>SnO<sub>4</sub>/G shows an improved electrochemical performance than bare Zn<sub>2</sub>SnO<sub>4</sub> due to the conducting, dispersing and immobilizing effects of graphene.

© 2012 Elsevier B.V. All rights reserved.

## 1. Introduction

Since reported by Idota et al. that tin-based amorphous oxide exhibited a stable capacity of over 600 mAh g<sup>-1</sup> [1], a renewed interest has turned to tin-based oxide anodes for Li-ion batteries. The theoretical capacity of SnO<sub>2</sub> can reach as high as 780 mAh g<sup>-1</sup> with the lithiation mechanism: SnO<sub>2</sub> + 4Li → Sn + 2Li<sub>2</sub>O, Sn + xLi ↔ Li<sub>x</sub>Sn ( $x \leq 4.4$ ) [2]. This material, however, suffers from a rapid capacity fade due to the large volume changes (358%) upon Li-insertion/extraction. It was found that nanostructured SnO<sub>2</sub> could exhibit an improved cycling stability compared to its bulk counterpart [3–9]. However, nanoparticles tend to aggregate upon repeated cycling. A practical strategy to overcome this problem is to load the nanoparticles onto a matrix. Improvement in electrochemical performance was observed when carbon materials were used as the matrices [10–15].

Compared with conventional carbon materials, graphene, a two-dimensional (2D) carbon material [16], is more attractive as a matrix to support SnO<sub>2</sub> nanoparticles. Recent research has shown that the electrochemical performance of SnO<sub>2</sub> could be significantly enhanced by anchoring it onto graphene [17–25]. The flexible graphene not only buffers the volume changes during Li-insertion/extraction processes but also prevents the aggregation of the nanoparticles upon long-term cycling due to its large specific surface area [26] and high mechanical strength [27]. Other merits by using graphene as the matrix include: (i) graphene with a high electronic conductivity [28] can serve as continuous conducting channels for the SnO<sub>2</sub> nanoparticles; (ii) graphene itself shows reversible Li-storage properties [29,30], which means that the introduction of graphene will not sacrifice the capacity of SnO<sub>2</sub> obviously.

Besides these simple tin oxides, some Sn-based mixed oxides M<sub>2</sub>SnO<sub>4</sub> (M = Mg [31,32], Co [32,33], Mn [32], and Zn [32,34]) with an inverse spinel structure are also potential anodes for Li-ion batteries. For Co<sub>2</sub>SnO<sub>4</sub>, an enhancement in electrochemical

\* Corresponding author. Tel.: +86 571 87952181; fax: +86 571 87951451.

E-mail address: [xiejian1977@zju.edu.cn](mailto:xiejian1977@zju.edu.cn) (J. Xie).

performance was realized either by using nanosized material [35] or by introducing a carbon matrix [36,37]. In the above mixed oxides,  $Zn_2SnO_4$  is received special interest because both Zn and Sn contribute to the overall capacity by forming Li–Zn and Li–Sn alloys [34]. To our best knowledge, however, there is no report about the effect of graphene on the electrochemical properties of  $Zn_2SnO_4$ . Herein, we report a facile one-pot *in situ* hydrothermal route to prepare  $Zn_2SnO_4$ -nanocrystals/graphene-nanosheets ( $Zn_2SnO_4/G$ ) nanohybrid. The electrochemical tests showed that the  $Zn_2SnO_4/G$  hybrid exhibits a obviously improved electrochemical performance compared with bare  $Zn_2SnO_4$ , indicating its promising application as anode for Li-ion batteries.

## 2. Experimental

### 2.1. Preparation of $Zn_2SnO_4/G$ nanohybrid

Graphite oxide (GO, 60 mg), prepared by a modified Hummer's method [38], was added into deionized (DI) water under sonication for 3 h to form a uniform solution. Then, 0.5 mmol of  $SnCl_4 \cdot 5H_2O$  and 1 mmol of  $ZnCl_2$  were mixed in DI water and added slowly into the above solution with stirring for 2 h. Afterwards, 4 mmol of  $N_2H_4 \cdot H_2O$  was added with stirring for another 0.5 h. The mixed solution was then transferred to a 100 mL Teflon-lined stainless steel autoclave and heated in an electric oven at 200 °C for 24 h. The resulting product was collected by centrifugation, washed with DI water and absolute ethanol for several times and dried at 60 °C under vacuum overnight. Bare  $Zn_2SnO_4$  was also synthesized with a similar route without adding GO.

### 2.2. Materials characterization

The crystal structures of the hydrothermal products were checked by X-ray diffraction (XRD) on a Rigaku D/Max-2550pc powder diffractometer equipped with Cu  $K_\alpha$  radiation ( $\lambda = 0.1541$  nm). The Raman spectra were recorded on a Jobin-Yvon Labour Raman HR-800 using Ar-ion laser of 514.5 nm. X-ray photoelectron spectroscopy (XPS) was collected on a KRATOS AXIS ULTRA-DLD spectrometer with a monochromatic Al  $K_\alpha$  radiation ( $h\nu = 1486.6$  eV). The morphologies of the products were observed by field emission scanning electron microscopy (FE-SEM) on a FEI-sirion microscope and transmission electron microscopy (TEM) on a JEM 2100F microscope. Thermogravimetric (TG) analysis was conducted on a DSCQ1000 instrument from 30 to 800 °C at a heating rate of 10 °C min<sup>-1</sup> under air.

### 2.3. Electrochemical measurements

The electrochemical performance of the hydrothermal products was evaluated by galvanostatic cycling using CR2025-type coin cells. The electrode slurry was made by dispersing 75wt.% active material ( $Zn_2SnO_4/G$ ,  $Zn_2SnO_4$ ), 15 wt.% acetylene black and 10 wt.% polyvinylidene fluoride (PVDF) in N-methyl pyrrolidone (NMP) with magnetic stirring for 2 h. The slurry was then coated onto Ni foam and dried at 100 °C under vacuum overnight to make the working electrodes. The electrodes were assembled into half cells in an Ar-filled glove box using Li foil as the counter electrode and Celgard 2300 membrane as the separator. The electrolyte used was 1 M  $LiPF_6$  in ethylene carbonate (EC)/dimethyl carbonate (DMC) (1:1 in volume). The cells were charged–discharged at various current densities between 0.005 and 3 V (vs. Li/Li<sup>+</sup>) on a Neware battery tester (Shenzhen, China). The capacity of  $Zn_2SnO_4/G$  is calculated based on the total mass of  $Zn_2SnO_4$  and graphene. All of the electrochemical measurements were carried out at 25 °C.

## 3. Results and discussion

Fig. 1a gives the XRD patterns of  $Zn_2SnO_4/G$  and  $Zn_2SnO_4$  prepared at 200 °C for 24 h. The dominant diffraction peaks can be indexed to cubic  $Zn_2SnO_4$  with a space group  $Fd\bar{3}m$  (JCPDS No.74–2184) for both samples. The small diffraction peak at  $2\theta = 27^\circ$  is the (110) peak of  $SnO_2$ . For  $Zn_2SnO_4/G$ , the characteristic peak of (002) plane of graphene, which should appear at  $2\theta = 25^\circ$ , cannot be clearly observed, due possibly to the low graphene content and/or the poor crystallization of graphene prepared by solution route.

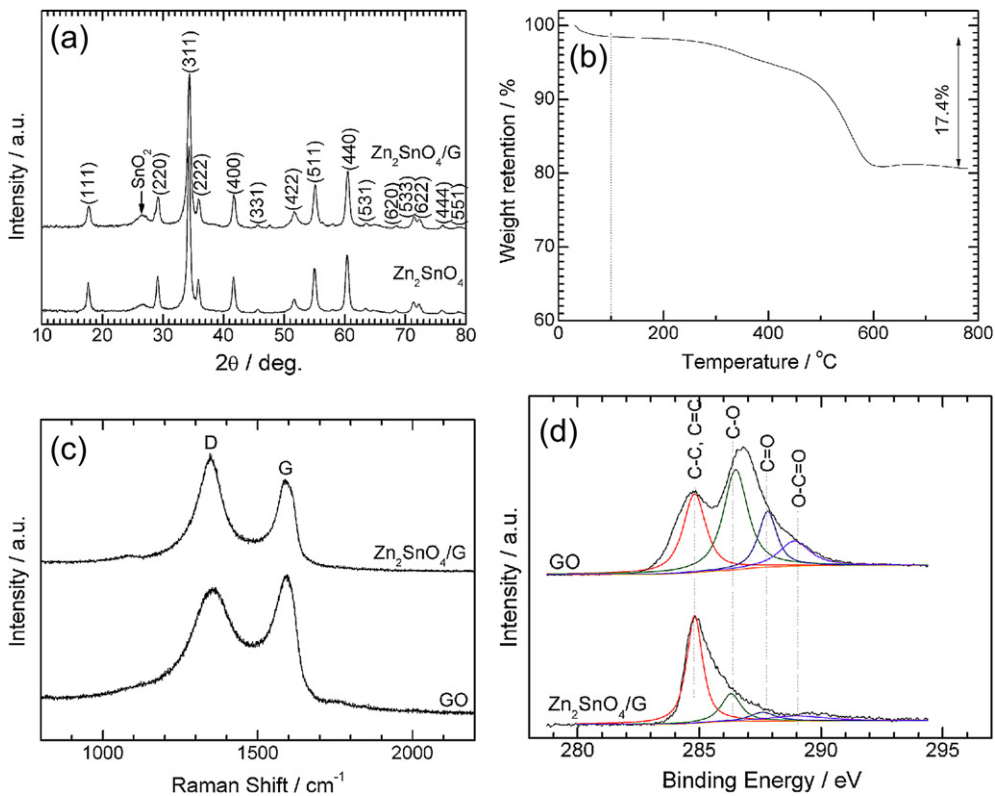
Fig. 1b shows the TG curve of  $Zn_2SnO_4/G$  in air between 30 and 800 °C. The weight loss before 100 °C is due to the loss of the absorbed water trapped within the graphene sheets [39]. The continuous weight loss between 100 and 800 °C signifies the removal of the residual oxygen-containing groups and the combustion of the carbon skeleton into carbon oxides. The graphene content in  $ZnFe_2O_4/G$  is estimated to be 17.4 wt.% based on the TG analysis. The weight of the absorbed water is excluded in the weight of graphene since  $ZnFe_2O_4/G$  will be dried at 100 °C under vacuum before the electrochemical tests.

The Raman spectra of  $Zn_2SnO_4/G$  and GO are presented in Fig. 1c. Note that both  $Zn_2SnO_4/G$  and GO exhibit two bands at 1350 and 1580 cm<sup>-1</sup>, corresponding to the D line and G Line, respectively, of carbon materials [40]. The G line is due to the  $E_{2g}$  phonon of the  $sp^2$  carbon atoms, while the D line is a breaking mode of  $\kappa$ -point phonons of  $A_{1g}$  symmetry [40,41]. As seen in the figure,  $Zn_2SnO_4/G$  displays an increased D-to-G intensity ratio compared with GO, which is due to the decrease of the average size of the  $sp^2$  domains during the reduction of GO [40]. Nevertheless, the number of the  $sp^2$  domains is increased during the reduction reactions [42]. The G peak exhibits an asymmetric feature. In fact, a D' peak appears on the shoulder of G peak (1620 cm<sup>-1</sup>). The D' peak is a defect peak related to the intra-valley scattering [43].

Besides the Raman spectra, XPS is another effective tool to monitor the reduction process of GO to graphene. Fig. 1d compares the C1s XPS spectra of  $Zn_2SnO_4/G$  and GO. The spectra can be deconvoluted into different forms of carbons:  $sp^2$ -hybridized graphitic carbon (C=C, 284.8 eV),  $sp^3$ -hybridized saturated carbon (C–C, 285.6 eV), carbon in C–O bonds (286.3 eV), carbonyl carbon (C=O, 287.6 eV) and carboxylate carbon (O–C=O, 289.0 eV) [44,45]. During the hydrothermal reactions using  $N_2H_4 \cdot H_2O$  as the reducing agent, the relative peak intensity of the oxygenated carbons (C–O, C=O, O–C=O) to non-oxygenated carbons (C–C or C=C) demonstrates a considerable decrease, which signifies the sufficient reduction of GO to graphene, in consistent with the Raman results.

Fig. 2a shows a typical SEM image of the  $Zn_2SnO_4/G$  hybrid. The hybrid exhibits a sheet structure composed of graphene and the anchored  $Zn_2SnO_4$ . The size of the sheet is as large as several microns. It is worth noting that almost all the  $Zn_2SnO_4$  particles are anchoring on graphene without forming free  $Zn_2SnO_4$  particles even though undergone vigorous ultrasonication treatment. This indicates that there is a strong interaction between  $Zn_2SnO_4$  and graphene. Fig. 2b shows the magnified SEM view of  $Zn_2SnO_4$ . Note that nanoscaled  $Zn_2SnO_4$  crystals are uniformly anchoring on the graphene sheets. From the edge of the  $Zn_2SnO_4/G$  hybrid, it is clear that the hybrid exhibits a layered structure constructed by alternatively arranged  $Zn_2SnO_4$  nanocrystals and graphene nanosheets as indicated by the arrows. Without the immobilization effect of graphene, the  $Zn_2SnO_4$  nanoparticles tend to aggregate as indicated in Fig. 3.

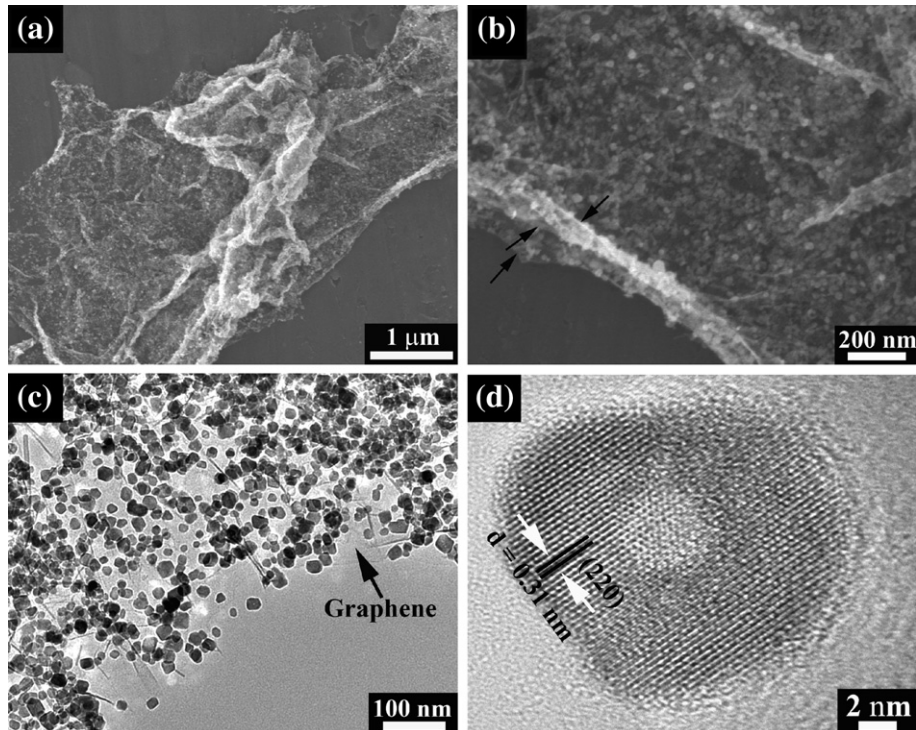
Fig. 2c shows a TEM image of the  $Zn_2SnO_4/G$  hybrid. It is clear that  $Zn_2SnO_4$  nanocrystals are uniformly anchored on graphene. The  $Zn_2SnO_4$  has a quasi-sphere shape with a size of 10–20 nm. It is suggested that the electrostatic attraction between the positively



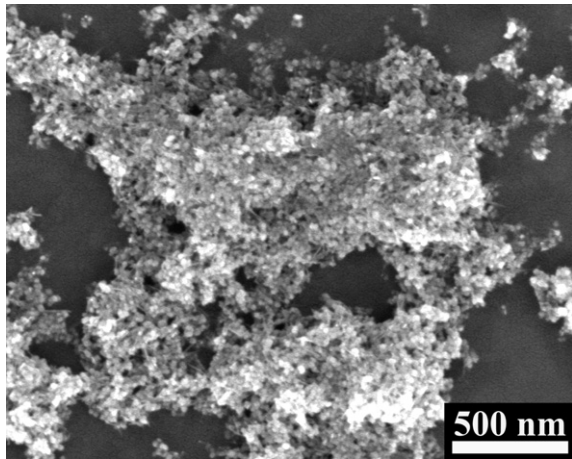
**Fig. 1.** (a) XRD patterns of Zn<sub>2</sub>SnO<sub>4</sub> and Zn<sub>2</sub>SnO<sub>4</sub>/G, (b) TG curve of Zn<sub>2</sub>SnO<sub>4</sub>/G, (c) Raman spectra of Zn<sub>2</sub>SnO<sub>4</sub>/G and GO and (d) C1s XPS of Zn<sub>2</sub>SnO<sub>4</sub>/G and GO.

charged metal ions (Zn<sup>2+</sup> and Sn<sup>4+</sup>) and the negatively charged graphene oxide sheets [46] in the precursors plays an important role in determining the uniform attachment of the Zn<sub>2</sub>SnO<sub>4</sub> nanocrystals on graphene in the final product. The transparent nature and the wrinkles in graphene also suggest that the graphene

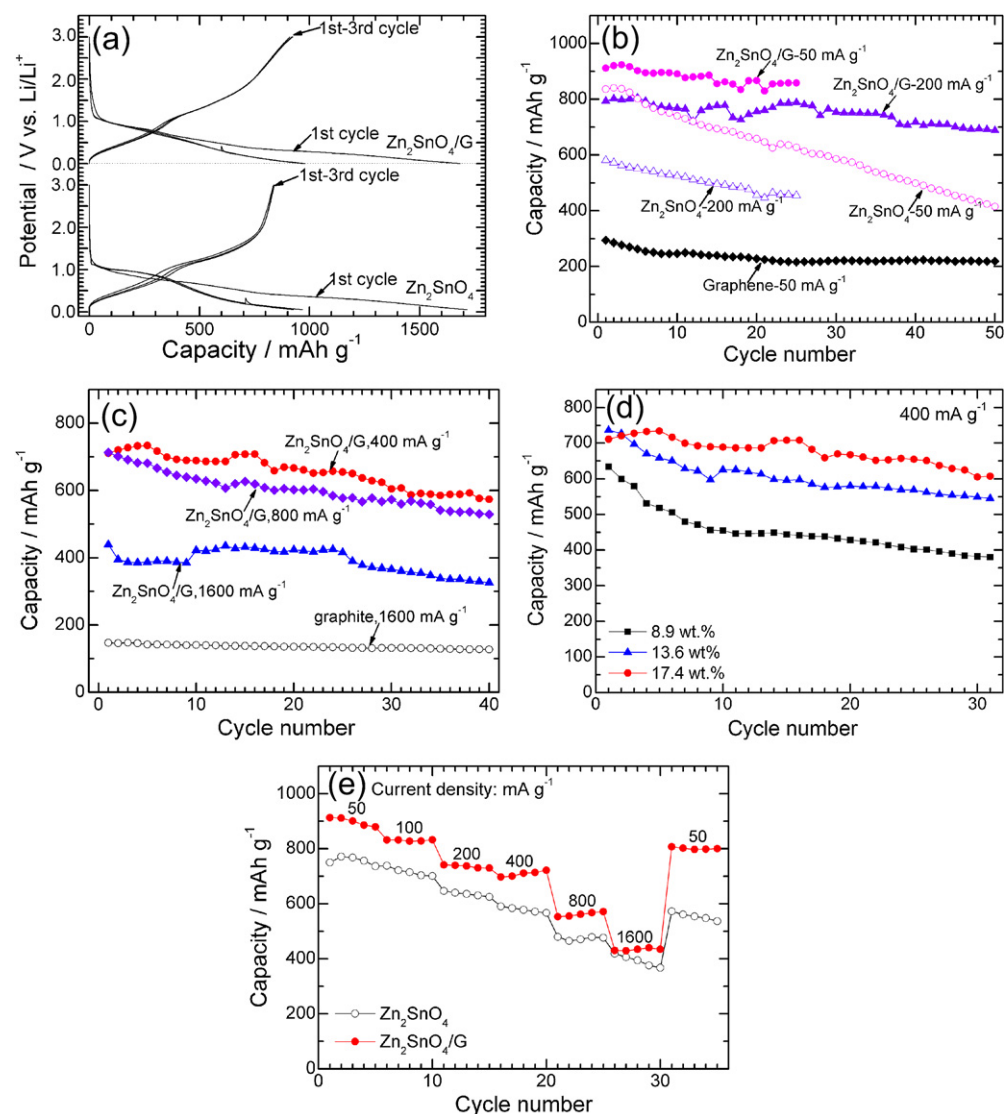
is rather thin consisted likely of few-layer sheets. Namely, it is well separated by the attached Zn<sub>2</sub>SnO<sub>4</sub> nanoparticles, agreeing well with the XRD results that the graphene in Zn<sub>2</sub>SnO<sub>4</sub>/G is undetectable by XRD even though it has a relatively high content (17.4 wt.%). Fig. 2d shows the lattice resolved high-resolution TEM (HRTEM)



**Fig. 2.** (a) Low-magnification SEM, (b) high-magnification SEM, (c) TEM and (d) HRTEM images of Zn<sub>2</sub>SnO<sub>4</sub>/G.



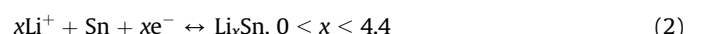
**Fig. 3.** SEM image of bare  $\text{Zn}_2\text{SnO}_4$ .

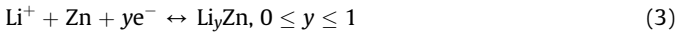


**Fig. 4.** (a) Voltage profiles of  $\text{Zn}_2\text{SnO}_4/\text{G}$  and  $\text{Zn}_2\text{SnO}_4$  charged–discharged at 50  $\text{mA g}^{-1}$ , (b) cycling performance of  $\text{Zn}_2\text{SnO}_4/\text{G}$  and  $\text{Zn}_2\text{SnO}_4$  charged at 50 and 200  $\text{mA g}^{-1}$  and discharged at 50  $\text{mA g}^{-1}$ , and bare graphene charged–discharged at 50  $\text{mA g}^{-1}$ , (c) cycling performance of  $\text{Zn}_2\text{SnO}_4/\text{G}$  charged at 400, 800 and 1600  $\text{mA g}^{-1}$  and discharged at 50  $\text{mA g}^{-1}$ , (d) cycling performance of  $\text{Zn}_2\text{SnO}_4/\text{G}$  with different graphene contents charged at 400  $\text{mA g}^{-1}$  and discharged at 50  $\text{mA g}^{-1}$ , and (e) rate capability of  $\text{Zn}_2\text{SnO}_4/\text{G}$  and  $\text{Zn}_2\text{SnO}_4$ .

image of an individual  $\text{Zn}_2\text{SnO}_4$  nanocrystal on graphene. The fringe spacing is measured to be 0.31 nm, corresponding to the interplanar spacing of (220) plane of  $\text{Zn}_2\text{SnO}_4$ . Therefore, it can be concluded from the XRD, Raman, XPS, SEM, TEM and HRTEM results that a  $\text{Zn}_2\text{SnO}_4/\text{G}$  hybrid has formed during this one-step *in situ* hydrothermal route.

Fig. 4a shows the voltage profiles of  $\text{Zn}_2\text{SnO}_4/\text{G}$  and  $\text{Zn}_2\text{SnO}_4$  for the first three cycles. The cells were charged–discharged at 50  $\text{mA g}^{-1}$  between 0.005 and 3 V. The capacity of  $\text{Zn}_2\text{SnO}_4/\text{G}$  is calculated based on the total weight  $\text{Zn}_2\text{SnO}_4$  and graphene, namely, the capacity per unit composite weight. The first charge (Li-extraction) and discharge (Li-insertion) capacities of  $\text{Zn}_2\text{SnO}_4$  are 836 and 1714  $\text{mAh g}^{-1}$ , respectively. The theoretical maximum capacity of  $\text{Zn}_2\text{SnO}_4$  is 547  $\text{mAh g}^{-1}$  according to the reaction mechanism proposed by Rong et al. [34]:





On the other hand, if Eq. (1) is completely reversible, the maximum capacity of  $\text{Zn}_2\text{SnO}_4$  is  $1231 \text{ mAh g}^{-1}$ . This means that Eq. (1) is reversible, at least partially, agreeing with the previous findings [34]. For  $\text{Zn}_2\text{SnO}_4/\text{G}$ , the first charge and discharge capacities are 911 and  $1685 \text{ mAh g}^{-1}$ , respectively. The high charge capacity of  $\text{Zn}_2\text{SnO}_4/\text{G}$  is likely attributed to the synergistic effect between  $\text{Zn}_2\text{SnO}_4$  nanocrystals and the conductive graphene. As seen in Fig. 4b, although bare graphene only gives a specific capacity below  $300 \text{ mAh g}^{-1}$ , the spacer effect of the anchored  $\text{Zn}_2\text{SnO}_4$  nanocrystals maximizes the contact of graphene with the electrolyte, which adds the capacity of graphene contributed by Li-ion absorption [47], besides the intercalation effect. For both samples, however, a large first irreversible is observed, due to the decomposition of the electrolyte and the formation of the solid electrolyte interface (SEI) [34].

Fig. 4b compares the cycling stability between  $\text{Zn}_2\text{SnO}_4/\text{G}$  and  $\text{Zn}_2\text{SnO}_4$ . The cells are charged at  $50$  and  $200 \text{ mA g}^{-1}$  and discharged at  $50 \text{ mA g}^{-1}$  over the voltage range of  $0.005$ – $3 \text{ V}$ . It is evident that  $\text{Zn}_2\text{SnO}_4/\text{G}$  exhibits an improved cycling stability compared with bare  $\text{Zn}_2\text{SnO}_4$ . The charge capacity of bare  $\text{Zn}_2\text{SnO}_4$  drops rapidly from  $836$  to  $406 \text{ mAh g}^{-1}$  after  $50$  cycles at  $50 \text{ mA g}^{-1}$ . For  $\text{Zn}_2\text{SnO}_4/\text{G}$ , a charge capacity of  $688 \text{ mAh g}^{-1}$  can still be retained after  $50$  cycles at  $200 \text{ mA g}^{-1}$ . The improved cycling stability can be ascribed to the buffering effect of the introduced graphene, which effectively alleviates the large volumes changes of  $\text{Zn}_2\text{SnO}_4$  upon Li-insertion/extraction. The large volume changes are responsible for the pulverization and exfoliation of the active materials, which lead to the failure of physical contact between the active materials and the current collector. In addition, the aggregation of the nanoparticles can be inhibited by the immobilization effect of graphene. The particles aggregation also contributes to loss of the physical contact with the current collector, causing a rapid capacity fade.

Fig. 4c gives the cycling stability of  $\text{Zn}_2\text{SnO}_4/\text{G}$  at high current densities. The cells are charged at  $400$ ,  $800$ , and  $1600 \text{ mA g}^{-1}$  and discharged at  $50 \text{ mA g}^{-1}$ . The initial charge capacities of  $\text{Zn}_2\text{SnO}_4/\text{G}$  at  $400$  and  $800 \text{ mA g}^{-1}$  can reach  $713$  and  $711 \text{ mAh g}^{-1}$ , respectively. The high charge capacity of  $\text{Zn}_2\text{SnO}_4/\text{G}$  at high current densities is due to the conductive effect of graphene, which enhances the electrode kinetics and increases the utilization of the active materials. After being cycled at  $800 \text{ mA g}^{-1}$  for  $40$  cycles, a charge capacity over  $500 \text{ mAh g}^{-1}$  is still maintained. For  $\text{Zn}_2\text{SnO}_4/\text{G}$ , a first charge capacity of  $439 \text{ mAh g}^{-1}$  can still be obtained at a current density as high as  $1600 \text{ mA g}^{-1}$ . This current density is over  $1 \text{ C}$ , even though considering the complete reversible reaction of Eq. (1). After  $40$  cycles at  $1600 \text{ mA g}^{-1}$ , a charge capacity over  $300 \text{ mAh g}^{-1}$  can be still kept, indicating the high-rate cycling stability of  $\text{Zn}_2\text{SnO}_4/\text{G}$ . Obviously, graphene plays a crucial role in determining the good cycling stability of  $\text{Zn}_2\text{SnO}_4/\text{G}$  at high current densities. For comparison, the cycling performance of natural graphite (the same sample used to make GO). It should be stressed that although natural graphite has a theoretical capacity of  $372 \text{ mAh g}^{-1}$ , it can deliver a charge capacity of only  $127 \text{ mAh g}^{-1}$  after  $50$  cycles at  $1600 \text{ mA g}^{-1}$ . As seen in Fig. 4c, the capacity of  $\text{Zn}_2\text{SnO}_4/\text{G}$  exhibits a fluctuation with cycling, due possibly to the pseudocapacitive character of the polymeric film [48].

Fig. 4d shows effect of graphene content on cycling stability  $\text{Zn}_2\text{SnO}_4$  charged at  $400 \text{ mA g}^{-1}$ . The other two  $\text{Zn}_2\text{SnO}_4/\text{G}$  samples are synthesized using the same procedure described above by adding  $20$  and  $40 \text{ mg GO}$  in the precursors, corresponding to graphene contents of  $8.9 \text{ wt.\%}$  and  $13.6 \text{ wt.\%}$ , respectively. Clearly,  $\text{Zn}_2\text{SnO}_4/\text{G}$  exhibits improved cycling stability with increasing graphene content especially in the initial cycles. It was found that

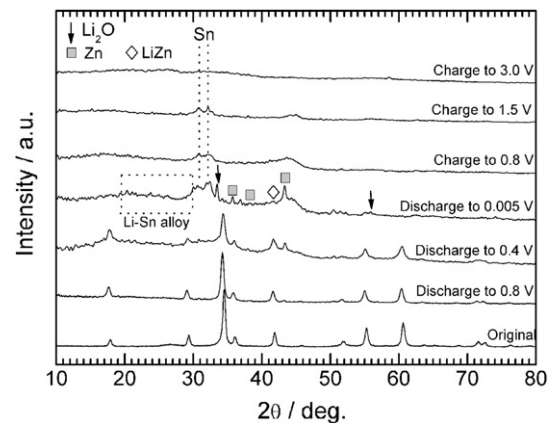


Fig. 5. Ex situ XRD of  $\text{Zn}_2\text{SnO}_4$  electrode at different charge–discharge states.

further increasing the graphene content cannot improve the cycling stability of  $\text{Zn}_2\text{SnO}_4$  obviously, but will increase the first irreversible capacity of the  $\text{ZnFe}_2\text{O}_4/\text{G}$  composite due to the large first irreversible capacity of bare graphene.

Fig. 4e compares the rate capability between  $\text{Zn}_2\text{SnO}_4/\text{G}$  and  $\text{Zn}_2\text{SnO}_4$ .  $\text{Zn}_2\text{SnO}_4/\text{G}$  shows a better rate capability than bare  $\text{Zn}_2\text{SnO}_4$ . It suggests that the improved rate capability comes mainly from two factors: first, the highly conductive graphene offers 2D conductive channels for the  $\text{Zn}_2\text{SnO}_4$  nanocrystals; second, the layered structure of  $\text{Zn}_2\text{SnO}_4/\text{G}$  hybrid facilitates the better wetting of the active materials by the electrolyte, leading to the faster Li-ion transport across the electrode/electrolyte interface. For  $\text{Zn}_2\text{SnO}_4/\text{G}$ , after being cycled at high current densities, the charge capacity can be recovered to a high value when the current density is shifted to a low value, indicating that the integrity of electrode can be kept during cycling by introducing graphene. By contrast, for bare  $\text{Zn}_2\text{SnO}_4$ , the recovery of the charge capacity cannot be fully realized upon decreasing the current density, suggesting that the electrode integrity has been destroyed after high-rate cycling.

The lithiation–delithiation mechanism of  $\text{Zn}_2\text{SnO}_4$  was investigated by ex situ XRD upon first discharge–charge cycle as shown in Fig. 5. Note that Sn, Zn, LiZn and Li–Sn phases form upon progressive Li uptake process. Meanwhile, the peak intensity of original  $\text{Zn}_2\text{SnO}_4$  is on the decrease during the discharge process, indicative of its decomposition upon Li uptake. When discharged to  $0.005 \text{ V}$ , the peaks of  $\text{Zn}_2\text{SnO}_4$  disappear with  $\text{Li}_2\text{O}$  and  $\text{LiZn}$  phases formed. The small peaks at  $2\theta = 20$ – $30^\circ$  are related to the various Li–Sn phases ( $\text{Li}_5\text{Sn}_2$ ,  $\text{Li}_{13}\text{Sn}_5$ ,  $\text{Li}_7\text{Sn}_2$ ,  $\text{Li}_{22}\text{Sn}_5$ ) [2]. The presence Sn and Zn at this potential indicates that the lithiation reactions of Sn and Zn cannot be fully completed even though at deep discharge state. When re-charged to  $0.8 \text{ V}$ ,  $\text{Li}_2\text{O}$ , Li–Sn alloys and  $\text{LiZn}$  phases disappear completely, indicating the decomposition of these phases upon Li-extraction, while the peak intensity of the residual Zn and Sn undergo a gradual decrease. At the charge potential of  $3 \text{ V}$ , all the diffraction peaks disappear, suggesting that Zn and Sn have been oxidized to  $\text{ZnO}$  and  $\text{SnO}_2$  in deep charge state. The absence of the  $\text{Zn}_2\text{SnO}_4$  (or the mixture of  $\text{ZnO}$  and  $\text{SnO}_2$ ) peaks implies that they are in an amorphous state, in contrast to the previous report [34], where  $\text{Zn}_2\text{SnO}_4$  peaks can still be observed upon full charge. The difference may be due to the rather small size of  $\text{Zn}_2\text{SnO}_4$  crystals in our  $\text{Zn}_2\text{SnO}_4/\text{G}$  sample.

#### 4. Conclusions

In summary, a layered  $\text{Zn}_2\text{SnO}_4/\text{G}$  nanohybrid has been successfully synthesized by a facile one-pot route. The  $\text{Zn}_2\text{SnO}_4$  nanocrystals with a size of  $10$ – $20 \text{ nm}$  are confined and dispersed by

the graphene sheets, forming a unique hybrid nanostructure. The  $\text{Zn}_2\text{SnO}_4/\text{G}$  nanohybrid shows better cycling stability and rate capability than bare  $\text{Zn}_2\text{SnO}_4$ . The enhancement in cycling stability is attributed to the incorporation of the flexible graphene sheets that act both as the buffer to alleviate the volume changes and as the separator to inhibit the aggregation of the  $\text{Zn}_2\text{SnO}_4$  particles. The nanohybrid also exhibits a good high-rate cycling stability. The incorporation of graphene also supplies 2D conductive channels for  $\text{Zn}_2\text{SnO}_4$  nanocrystals and maximizes their exposure to the electrolyte, leading to the improved rate capability. The good electrochemical performance of  $\text{Zn}_2\text{SnO}_4/\text{G}$  makes it a promising anode material for Li-ion batteries.

## Acknowledgements

This work was supported by the National Natural Science Foundation of China (No. 51101139), the Ph.D. Programs Foundation of Ministry of Education of China (No. 20100101120024), the Foundation of Education Office of Zhejiang Province (No. Y201016484), the Qianjiang Talents Project of Science Technology Department of Zhejiang Province (2011R10021), and Key Science and Technology Innovation Team of Zhejiang Province under grant number 2010R50013.

## References

- [1] Y. Idota, T. Kubota, A. Matsufuji, Y. Maekawa, T. Miyasaka, *Science* 276 (1997) 1395–1397.
- [2] I.A. Courtney, J.R. Dahn, *J. Electrochem. Soc.* 144 (1997) 2045–2052.
- [3] C. Kim, M. Noh, M. Choi, J. Cho, B. Park, *Chem. Mater.* 17 (2005) 3297–3301.
- [4] D. Deng, J.Y. Lee, *Chem. Mater.* 20 (2008) 1841–1846.
- [5] M.S. Park, Y.M. Kang, G.X. Wang, S.X. Dou, H.K. Liu, *Adv. Funct. Mater.* 18 (2008) 455–461.
- [6] H.B. Wu, J.S. Chen, X.W. Lou, H.H. Hng, *J. Phys. Chem. C* 115 (2011) 24605–24610.
- [7] J.P. Liu, Y.Y. Li, X.T. Huang, R.M. Ding, Y.Y. Hu, J. Jiang, L. Liao, *J. Mater. Chem.* 19 (2009) 1859–1864.
- [8] P. Meduri, C. Pendyala, V. Kumar, G.U. Sumanasekera, M.K. Sunkara, *Nano Lett.* 9 (2009) 612–616.
- [9] X.W. Lou, Y. Wang, C.L. Yuan, J.Y. Lee, L.A. Archer, *Adv. Mater.* 18 (2006) 2325–2329.
- [10] X.W. Lou, D. Deng, J.Y. Lee, L.A. Archer, *Chem. Mater.* 20 (2008) 6562–6566.
- [11] X.W. Lou, J.S. Chen, P. Chen, L.A. Archer, *Chem. Mater.* 21 (2009) 2868–2874.
- [12] X.W. Lou, C.M. Li, L.A. Archer, *Adv. Mater.* 21 (2009) 2536–2539.
- [13] Y. Wang, H.C. Zeng, J.Y. Lee, *Adv. Mater.* 18 (2006) 645–649.
- [14] C.H. Xu, J. Sun, L. Gao, *J. Phys. Chem. C* 113 (2009) 20509–20513.
- [15] J.G. Kim, S.H. Nam, S.H. Lee, S.M. Choi, W.B. Kim, *ACS Appl. Mater. Interfaces* 3 (2011) 828–835.
- [16] K.S. Novoselov, A.K. Geim, S.V. Morozov, D. Jiang, Y. Zhang, S.V. Dubonos, I.V. Grigorieva, A.A. Firsov, *Science* 306 (2004) 666–669.
- [17] S.J. Ding, D.Y. Luan, F.Y. Chiang Boey, J.S. Chen, X.W. Lou, *Chem. Commun.* 47 (2011) 7155–7157.
- [18] J.X. Zhu, Z.Y. Lu, M.O. Oo, H.H. Hng, J. Ma, H. Zhang, Q.Y. Yan, *J. Mater. Chem.* 21 (2011) 12770–12776.
- [19] S. Baek, S.H. Yu, S.K. Park, A. Pucci, C. Marichy, D.C. Lee, Y.E. Sung, Y.Z. Piao, N. Pinna, *RSC Adv.* 1 (2011) 1687–1690.
- [20] H. Kim, S.W. Kim, Y.U. Park, H. Gwon, D.H. Seo, Y. Kim, K. Kang, *Nano Res.* 3 (2010) 813–821.
- [21] C. Zhong, J.Z. Wang, Z.X. Chen, H.K. Liu, *J. Phys. Chem. C* 115 (2011) 25115–25120.
- [22] S.M. Paek, E. Yoo, I. Honma, *Nano Lett.* 9 (2009) 72–75.
- [23] B. Zhang, Q.B. Zheng, Z.D. Huang, S.W. Oh, J.K. Kim, *Carbon* 49 (2011) 4524–4534.
- [24] P.C. Lian, X.F. Zhu, S.Z. Liang, Z. Li, W.S. Yang, H.H. Wang, *Electrochim. Acta* 56 (2011) 4532–4539.
- [25] X.J. Zhu, Y.W. Zhu, S. Murali, M.D. Stoller, R.S. Ruoff, *J. Power Sources* 196 (2011) 6473–6477.
- [26] M.D. Stoller, S. Park, Y.W. Zhu, J.H. An, R.S. Ruoff, *Nano Lett.* 8 (2008) 3498–3502.
- [27] C. Lee, X.D. Wei, J.W. Kysar, J. Hone, *Science* 321 (2008) 385–388.
- [28] S. Park, J.H. An, I.W. Jung, R.D. Piner, S.J. An, X.S. Li, A. Velamakanni, R.S. Ruoff, *Nano Lett.* 9 (2009) 1593–1597.
- [29] E. Yoo, J. Kim, E. Hosono, H.S. Zhou, T. Kudo, I. Honma, *Nano Lett.* 8 (2008) 2277–2282.
- [30] D.Y. Pan, S. Wang, B. Zhao, M.H. Wu, H.J. Zhang, Y. Wang, Z. Jiao, *Chem. Mater.* 21 (2009) 3136–3142.
- [31] T. Xiao, Y.W. Tang, Z.Y. Jia, S.L. Feng, *Electrochim. Acta* 54 (2009) 2396–2401.
- [32] P.A. Connor, J.T.S. Irvine, *J. Power Sources* 97–98 (2001) 223–225.
- [33] P.A. Connor, J.T.S. Irvine, *Electrochim. Acta* 47 (2002) 2885–2892.
- [34] A. Rong, X.P. Gao, G.R. Li, T.Y. Yan, H.Y. Zhu, J.Q. Qu, D.Y. Song, *J. Phys. Chem. B* 110 (2006) 14754–14760.
- [35] G. Wang, X.P. Gao, P.W. Shen, *J. Power Sources* 192 (2009) 719–723.
- [36] Y. Qi, N. Du, H. Zhang, P. Wu, D.R. Yang, *J. Power Sources* 196 (2011) 10234–10239.
- [37] G. Wang, Z.Y. Liu, P. Liu, *Electrochim. Acta* 56 (2011) 9515–9519.
- [38] W.S. Hummers, R.E. Offeman, *J. Am. Chem. Soc.* 80 (1958) 1339.
- [39] S. Dubin, S. Gilje, K. Wang, V.C. Tung, K. Cha, A.S. Hall, J. Farrar, R. Varshneya, Y. Yang, R.B. Kaner, *ACS Nano* 4 (2010) 3845–3852.
- [40] F. Tuinstra, J.L. Koenig, *J. Chem. Phys.* 53 (1970) 1126–1130.
- [41] A.C. Ferrari, J. Robertson, *Phys. Rev. B* 61 (2000) 14095–14107.
- [42] S. Stankovich, D.A. Dikin, R.D. Piner, K.A. Kohlhaas, A. Kleinhammes, Y.Y. Jia, Y. Wu, S.T. Nguyen, R.S. Ruoff, *Carbon* 45 (2007) 1558–1565.
- [43] A.C. Ferrari, *Solid State Commun.* 143 (2007) 47–57.
- [44] H.J. Shin, K.K. Kim, A. Benayad, S.M. Yoon, H.K. Park, I.S. Jung, M.H. Jin, H.K. Jeong, J.M. Kim, J.Y. Choi, Y.H. Lee, *Adv. Funct. Mater.* 19 (2009) 1987–1992.
- [45] T.K. Hong, D.W. Lee, H.J. Choi, H.S. Shin, B.S. Kim, *ACS Nano* 4 (2010) 3861–3868.
- [46] D. Li, M.B. Müller, S. Gilje, R.B. Kaner, G.G. Wallace, *Nat. Nanotechnol.* 3 (2008) 101–105.
- [47] J.R. Dahn, T. Zheng, Y.H. Liu, J.S. Xue, *Science* 270 (1995) 590–593.
- [48] S. Laruelle, S. Grugeon, P. Poizot, M. Dollé, L. Dupont, J.M. Tarascon, *J. Electrochem. Soc.* 149 (2002) A627–A634.